International Journal of Thermofluid Science and Technology (2022)
Volume 9, Issue 5, Paper No. 090502
https://doi.org/10.36963/IJTST.2022090502

Research Article

Numerical investigation on VIV energy harvesting enhancement with adding eccentricity to a circular cylinder

Zahra Babaie, Foad Moslem, Mehran Masdari*, Mojtaba Tahani

Faculty of New Sciences and Technologies, University of Tehran, North Kargar Street, Tehran, 14395-1561, Iran

ATICLE INFO

Received: 28 June 2022;
Received in revised form:
15 Aug. 2022;
Accepted: 18 Aug. 2022;
Published online:
28 Aug. 2022

Keywords:
Energy harvesting
Vortex-induced vibration (VIV)
Rotating cylinder
Finite-element method
Numerical simulation

ABSTRACT

In recent years, energy harvesting from vortex-induced vibration (VIV) of a cylinder as a renewable source of energy has been increased. The main goal is to enhance the harnessed hydrokinetic energy of the VIV converters. In this work, the effect of adding a rotational degree of freedom by giving eccentricity to the circular cylinder is investigated on vibration and rotational response as well as hydrokinetic energy conversion. Simulations are done at the Reynolds number ranging from 2×10^3 to 13×10^3. Two-dimensional unsteady Reynolds-averaged Navier–Stokes equations (URANS), supplemented with SST turbulence models, are solved on moving mesh, and arbitrary Lagrangian-Eulerian formulation is employed to accommodate the deforming boundaries. For the freely rotating and vibrating cylinder, results demonstrate that increasing the inlet velocity increases the vibration amplitude, and the cylinder experiences complete rotation in some of the flow times. Moreover, adding a rotational degree of freedom causes hydrodynamic instability, in which the location of separation points changes and makes a wide wake pattern with unstable vortexes behind the cylinder. As a result, the harnessed power and energy conversion efficiency of the system is increased. The freely vibrating-rotating system generates a maximum power of 0.024 (W), and the energy conversion efficiency increases and fluctuates around 11.2%.

1. Introduction

In the last decades, global energy demand has risen due to the rapid development of the population. The depletion of traditional energy sources, such as fossil fuels, and their adverse effects on the environment have led the global community to seek alternative energy, especially renewable energy resources [1]. Capturing renewable energy from the wave [2, 3], tidal current [4], and other water resources are gaining more importance. As renewable energy conversion technologies are developing, many different energy converters have been built to harvest renewable energy [5]. In 2008, Bernitsas and Raghavan [6] invented the device called VIVACE to convert ocean or river current energy to electricity.

*Corresponding e-mail: m.masdari@ut.ac.ir (Mehran Masdari)

This converter's basic unit is an elastically mounted rigid cylinder and can harness the current's power in velocity even below 0.4 m/s [7].

Nomenclature

u_{in}	Inlet velocity (m/s)	y	Cylinder displacement (m)
ρ	Density of fluid (kg/m^3)	$\dot{y}$	Cylinder velocity (m/s)
$U*$	Reduced velocity $U^* = u_{\mathrm{in}}/Df_{\mathrm{n}}$	$\ddot{y}$	Cylinder acceleration (m/s^2)
Re	Reynolds number $Re = \rho u_{in} D/\mu$	$f(t)$	Fluid force acting on the cylinder
D	Diameter of the cylinder (m)	e	Eccentricity $e = D/4$
L	Length of the cylinder (m)	I	Moment of inertia $I = \frac{1}{2}m(D/2)^2 + me^2$ (kg m^2)
m	Total mass (kg)	θ	Rigid body rotation (rad)
m_d	Displaced mass $\pi\rho D^2 L/4$ (kg)	$\dot{\theta}$	Angular velocity (rad/s)
m^*	Mass ratio $m^* = m/m_a$	$\ddot{\theta}$	Angular acceleration (rad/s^2)
f_n	Natural frequency $\mathrm{f_n} = \sqrt{\mathrm{k}/(\mathrm{m}+\mathrm{m_d})}/\ 2\pi$ (Hz)	$M(t)$	Torque acting on the cylinder
f^*	Frequency ratio (f/f_n)	t_s	Steady time (s)
c	System damping (N · s/m)	T	Oscillation period (1/s)
k	Spring stiffness (N/m)	A^*	Non-dimensional amplitude (y/D)
ζ	Damping ratio $\zeta = c/\ 2\sqrt{k(m+m_d)}$	A_S	Amplitude of spectrum
$(\overline{CD})$	Mean drag coefficient	FFT	Fast Fourier Transformation
$C_{l_{RMS}}$	Root mean square lift coefficient	$P1$	Power of vibration (W)
t^*	Non-dimensional time $t^* = u_{in}t/D$	P_{tot}	Total power of vibration and rotation (W)
η	Efficiency $\eta = P_{tot}/\ P_{fluid}$	P_{fluid}	Power in the fluid (W)

Shedding vortices behind the flexibly mounted cylinder apply periodic hydrodynamic loads which may induce the structure's vibration. This interaction between fluid and structure is called Vortex-Induced Vibration (VIV), which is a form of Flow-Induced Motions (FIM) [8]. Vortex-induced vibration of the circular cylinder occurs in all Reynolds numbers (Re) greater than 400 except in the transition region from laminar to turbulent [9]. Extensive research considering the vibration response of circular cylinder are summarized in the comprehensive reviews [10-12]. Khalak and Williamson [13, 14] experimentally investigated the low mass-damper parameter elastically mounted rigid cylinder oscillating in the crossflow direction. Their results identified four distinct region responses denoted as an initial excitation region, the "upper branch," the "lower branch," and the desynchronization region when the amplitude is plotted over normalized velocity. However, numerical results cannot match the experimental results in the upper branch (lock-

in) region at higher Re numbers since they are not able to capture the exact vortex shedding pattern [15]. Studying the wake regime showed that the different modes of vortex shedding depend on some key parameters, such as the reduced velocity and the cylinder mass [16]. Many different studies have also examined the impact of mass-ratio, damping, and stiffness on the VIV response of a cylinder [17-20]. Besides reduced velocity and the system's characteristics, adding a degree of freedom was considered in various research as a factor affecting the VIV response of the system. Jauvtis and Williamson [21] experimentally investigated the VIV of the cylinder in two-degree freedom. According to their study, the amplitude response resulted in remarkable changes for a mass ratio below six. VIV of free to move in both in-line and transverse cylinders were studied with direct numerical simulation [22, 23] and large eddy simulation [24] in subcritical Reynolds number regimes. These studies demonstrated that there is a difference between the VIV responses for the cylinder in line and crossflow motion and their one-degree-of-freedom counterparts at the intermediate reduced velocities.

Not only adding the translational degree of freedom but also the rotational degree of freedom is important while dealing with a VIV system. Various research numerically [25] and experimentally [26, 27] considered the effect of forced rotating and free crossflow vibrating a cylinder on VIV responses. Mittal [25] investigated the effect of eccentricity on translating and imposed rotating a cylinder with computational fluid dynamics for Re=5, 200, and 3800. In addition to the forced rotation, vortex-induced rotation (VIR) of bluff bodies is an essential issue in the application of engineering. Srigrarom and Koh [26] studied the self-excited rotational oscillation of a pivoted triangular cylinder under the uniform flow and visualized the flow patterns interchanging over a flat plate with particle image velocity (PIV) measurements. On the other hand, Lu et al. [27] numerically studied the flow-induced rotary oscillation of a cylinder for different splitter plate lengths. They showed that the simultaneous influence of the fluid moment, rotation response, and phase difference results in various natural frequencies of the rotating body and, consequently, a wide regime of synchronization. In 2019, Wang et al. [28] conducted a study on vortex-induced vibration of an elliptical cylinder which is free to vibrate at transverse and azimuthal directions simultaneously. Their results demonstrated that free rotation considerably affects the lift, drag, and momentum coefficients. Of course, investigation on VIV and VIR is not a new topic, but a little research has been focused on the combined effect of free rotation and free vibration.

Previously, VIV generally was considered a destructive phenomenon because of causing fatigue damage to the structures. However, in recent years, the approach to the VIV has been changed, and it is used as a source of energy. From the aspect of energy harvesting, it is desirable to enhance the oscillation amplitude of a cylinder and maintain a high vibration response. Barrero-Gill et al. [29] studied the impact of parameters like mass ratio (m^*) and the mechanical damping (ζ) on the VIV of a one-degree freedom cylinder as a factor of energy conversion. Their analysis revealed that there is an optimum value for $m^*\zeta$ to have a maximum efficiency. Also, the impact of the elastic modulus of the material, mass ratio, and cross-sectional was investigated for wide ranges of Reynolds number from 2000 to 50000 [30]. These parameters are considered as important factors affecting the VIV performance and, consequently, energy harvesting from a cylinder. The effect of the cylinder's cross-sections was separately investigated numerically and experimentally on energy conversion efficiency [31-35]. Due to the impact of rotational degree of freedom on VIV response, Zhu and Gao [36] and Zhu et al. [37] proposed a free-to-rotate impeller attached to the cylinder and numerically analyzed the effect of a freely rotating impeller on amplitude response and energy harnessing. They showed that the impeller increases the hydrodynamic instability resulting in enhancement of the in-line vibration and power.

Since both the vibration and rotation of the cylinder are capable of generating power, why not use a simple way to combine them? In this paper, an eccentric circular cylinder, as shown

in Fig. 1, was applied to harvest the energy from the fluid current. The cylinder was let move in a transverse direction and rotate freely. The configuration of the system is a freely rotating eccentric cylinder, linear spring, and damper. Suppose we assume the zero friction at power taken off (PTO) connection with the same energy harvesting system. In that case, the costs may not variate too much by adding eccentricity to the cylinder. Here come questions. How adding a degree of freedom will change the vibrating response? How much energy can be harvested by the eccentric rotating cylinder? Whether the energy conversion efficiency will increase significantly or not? So, it is worth investigating these questions before the real applications.

This study aims to find how the freely vibrating-rotating circular cylinder affects the vibrating response of one degree of freedom cylinder and how much power can harness by the converter. Time-dependent Navier-Stokes equations supplemented with a shear stress transport turbulence model are solved on a structural moving mesh, and boundaries allow to displace and rotate due to the cylinder's motion. Amplitude and frequency responses of the vibrating cylinder (1D) are validated with the previous experimental and numerical studies. Finally, the effect of adding a rotational degree of freedom on the VIV responses, generated power, and efficiency of the system is discussed. In summary, investigating the effect of combining the transverse vibration and free rotation with a simpler way, employing an eccentric circular cylinder, on VIV response and energy conversion efficiency of the converter at high Reynolds numbers is the contribution of this paper into the subject.

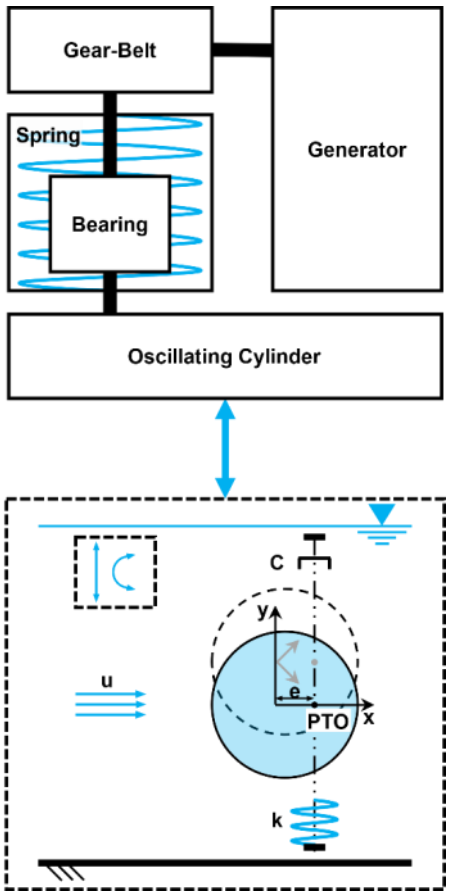

Fig. 1. A VIV energy harvesting system, and its simple schematic.

2. Physical Model Description

The simplified physical model of the free rotating-vibrating cylinder in a crossflow direction is depicted in Fig. 2(a). The oscillatory system consists of a solid cylinder, linear springs of stiffness "k , and linear structural damping "c. The cylinder can vibrate in the transverse direction, and the rotational degree of freedom is provided by attaching to the spring and damper with an eccentricity of $e = D/4$ to the PTO connection. The mass ratio of the system is m^*=2.4 ($m^* = m/m_d$), where m is the total structural mass, and m_d is displaced mass of fluid). The natural frequency of the circular cylinder is set as $f_n = \sqrt{k/(m+m_d)}/2\pi$ = 0.4 Hz. The value of $m^*\zeta$ is considered 0.014 based on Khalak and Williamson [14], where the damping ratio is defined by $\zeta = c/2\sqrt{k(m+m_d)}$.

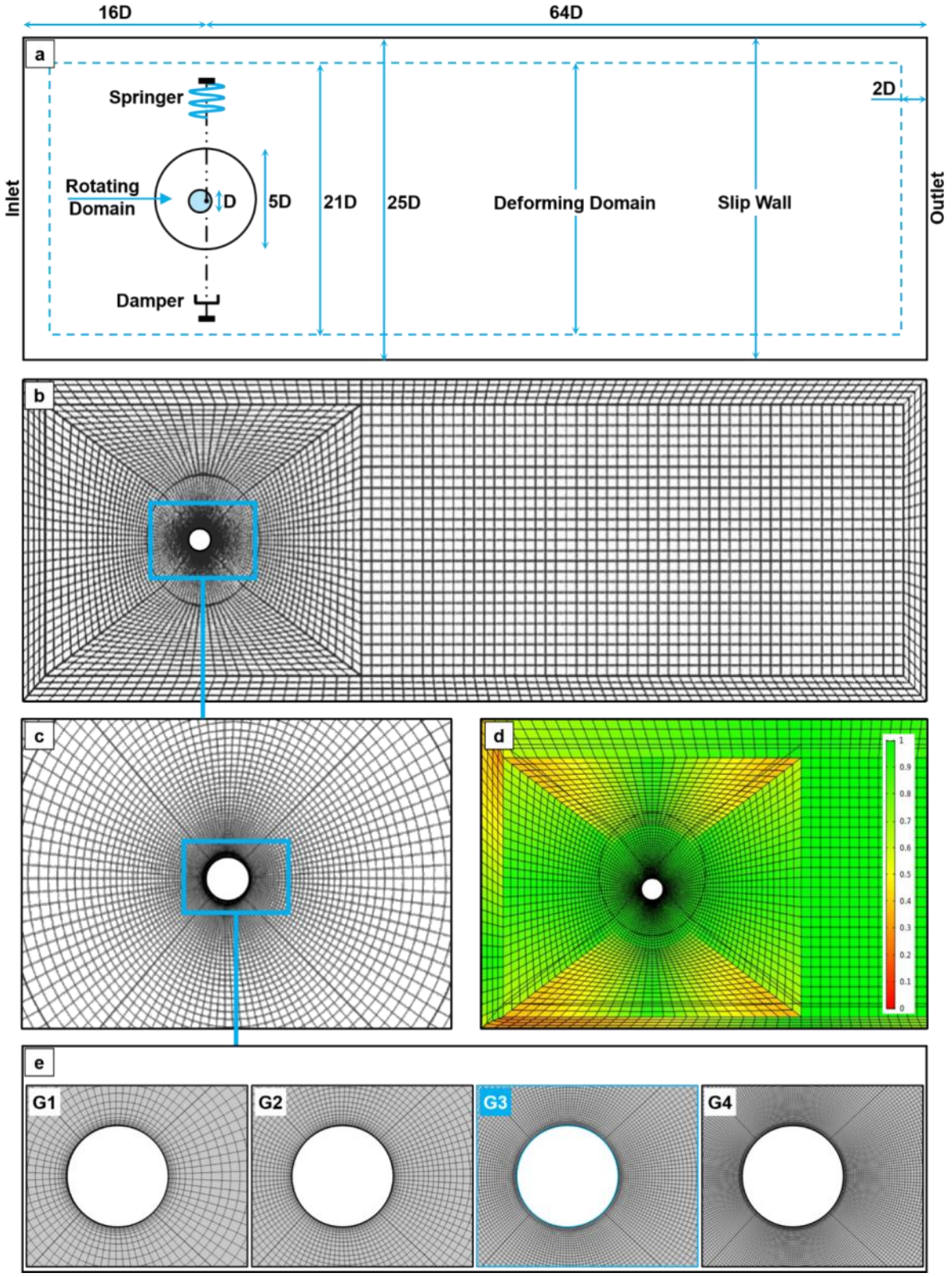

Fig. 2. (a) Computational domain and boundary conditions; (b) Computational mesh - whole domain; (c) Computational mesh - near cylinder; (d) Computational mesh after deformation; (e) Mesh independency study.

For examining the flow rate effect (u_{in}), the reduced velocity $U^* = u_{in}/Df_n$ is considered at ranges from 3 to 14 in which the inlet velocities vary from 0.06 to 0.29 (m/s). The simulation parameters are listed in Table 1.

Table 1 Physical model parameters.

Diameter	D [mm]	50.8
Length of The Cylinder	L [mm]	381
Mass Ratio	m^*	2.4
Total Structural Mass	m [kg]	1.8517
Spring Stiffness	k $[N/m]$	16.57
Structural Damping	c $[Ns/m]$	0.076916
Displaced Mass	m_d [kg]	0.77153
Natural Frequency	f_n [Hz]	0.4
Dynamic Viscosity of Water	μ $[N*s/m^2]$	0.0011379
Water Density	ρ $[kg/m^3]$	999.1026
Moment of Inertia at The Center of Rotation	I [kg.m^2]	8.9597E-4

As shown in Fig. 2(a), a rectangle region $80D \times 25D$ in the streamwise and crossflow direction is considered as a computational domain. The cylinder is placed at $16D$ downstream of the inlet in the middle of the channel. The three-dimensional simulation of VIV of the rotating-vibrating system is complicated and time-consuming, so these simulations are investigated primarily with two-dimensional simulation and provide reasonable predictions [37]. In order to reduce computational time, the domain is divided into three subdomains: rotating, deforming, and static domains. A circular zone around the cylinder (rotating domain) with a diameter of $5D$ pursues the rotational motion of the system while the outer rectangle zone (deforming domain) with the size of $2D$ follows the translational motion of the system. These zones can adapt in accordance with the motion of the object. In the static domain, the mesh is in the rest and remains unaltered during the computational process. This technique provides a hint for the mesh to deform using bilinear interpolation to compute the solution on deforming subdomain and coupling to the solution of the rotating subdomain. The flow continuity is considered between subdomains, and prescribed deformation is applied to both deforming and rotating domains.

The boundary conditions are also presented in Fig. 2(a). The normal velocity and zero-pressure-gradient are considered as upstream and downstream boundary conditions, respectively. The length of the domain is considered far from the cylinder to reach zero gradients for velocity ($\partial u/\partial x = 0, \partial v/\partial x = 0$) at the outlet. The slip-wall condition is given on the upper and lower boundaries, and on the surface of the cylinder, the no-slip condition is specified.

3. Computational Model and Numerical Approach

In this present study, two-dimensional Navier-Stocks equations coupled with (SST) $k-\omega$ turbulence model is applied to describe the flow field around the cylinder. The full incompressible Navier-Stokes with an Arbitrary-Lagrangian-Eulerian (ALE) [38] formulation are

$$\rho\frac{\partial \mathbf{u}}{\partial t} + \rho\big((\mathbf{u}-\mathbf{u}_m).\nabla\big)\mathbf{u} = \nabla.[-p\mathbf{I} + (\mu+\mu_T)(\nabla\mathbf{u}+\nabla\mathbf{u}^T)] + F \quad (1)$$

$$\nabla.\mathbf{u} = 0 \quad (2)$$

Where, $\mathbf{u} = (u, v)$ shows the velocity field, t the time, ρ the density, p the pressure , (μ, μ_T) the laminar and turbulent viscosity function. I denotes the unit diagonal matrix and $[\ ]^T$ the transpose of a matrix, and F is the volume force affecting the fluid. The mesh movement velocity is $\mathbf{u}_m = (u_m, v_m)$. In ALE formulation, $\mathbf{u}_m$ is determined by solving an equation for mesh displacement. This equation smoothly deforms the mesh given the constraints placed on the boundaries. Here, the Winslow smoothing method (Eq.3) is employed to create a single coupled system of equations for all coordinate directions, where x and y are spatial coordinates of the spatial frame, X_m and Y_m are the reference coordinates of the material frame.

$$\frac{\partial^2 X_m}{\partial x^2} + \frac{\partial^2 X_m}{\partial y^2} = 0 \qquad \frac{\partial^2 Y_m}{\partial x^2} + \frac{\partial^2 Y_m}{\partial y^2} = 0 \quad (3)$$

The SST turbulence model proposed by Menter [39] calculates two variables of the turbulent kinetic energy, k (Eq.4) and the dissipation rate of the eddies, ω (Eq.5). This model has demonstrated to give a good performance in capturing turbulent vortices and modeling flow with adverse pressure gradient [36, 40].

$$\rho\frac{\partial k}{\partial t}+\rho\mathbf{u}.\nabla k=\mathbf{P}-\rho\beta_0^*k\omega+\nabla.((\mu+\sigma_k\mu_T)\nabla k) \quad (4)$$

$$\rho\frac{\partial \omega}{\partial t}+\rho\mathbf{u}.\nabla\omega=\frac{\rho\gamma}{\mu_T}\mathbf{P}-\rho\beta\omega^2+\nabla.\left((\mu+\sigma_\omega\mu_T)\nabla\omega\right)+2(1-f_{v1})\frac{\rho\sigma_{\omega2}}{\omega}\nabla\omega.\nabla k \quad (5)$$

Where, $\mathbf{P}=\min(\mathrm{P}_k,10\rho\beta_0^*k\omega)$, in which P_k is a productive term defined by

$$P_k=\mu_T\left(\nabla\mathbf{u}:(\nabla\mathbf{u}+\nabla\mathbf{u}^T)-\frac{2}{3}(\nabla.\mathbf{u})^2\right)-\frac{2}{3}\rho k\nabla.\mathbf{u} \quad (6)$$

The turbulent viscosity is given by $\mu_T=\rho a_{1k}/\max(a_{1\omega},Sf_{v2})$ where S ($S=\sqrt{2S_{ij}S_{ij}}$) is the characteristic magnitude of the mean velocity gradient. $\beta,\gamma,\sigma_k,\sigma_\omega$ are model constant, evaluated from reference [39]. The model constants are defined through interpolation of appropriate inner and outer values, f_{v1} and f_{v2} are blending function [41].

$$\varphi=f_{v1}\varphi_1+(1-f_{v1})\varphi_2 \quad \text{for } \varphi=\beta,\gamma,\sigma_k,\sigma_\omega \quad (7)$$

Vortex-induced vibration of an eccentric cylinder can be described by the classical oscillator model of mass-spring-damper. The total hydrodynamic force of $F(t)=-(c\dot{y}(\mathrm{t})+ky\ (t))$ applied at the center of the rotation in a vertical direction on a cylinder with a mass of m. Value of transverse displacement (y(t)) and velocity ($\dot{y}(t)$) of the system continuously are calculated at each time step and replaced as initial values for the next time step. Assuming the zero friction at the center of the rotation for the freely rotating-vibrating system, the transverse motion will induce the rotational motion on the cylinder.

Commercially available finite element package COMSOL Multiphysics® version 5.4 is used to solve governing equations. The equations are discretized on structured Mapped meshes, as shown in Fig. 2(b,c) For the discretization of the fluids, the scheme of P2+P1, quadratic shape functions for the velocity but linear basis functions for the pressure, has been chosen. For establishing the Courant–Friedrichs–Lewy (CFL) condition, the non-dimensional time-step ($u_{in}\Delta t/D$) is set to be 0.01, and keep the CFL number smaller than one. The fix-stepsize Backward Differentiation Formula (BDF) method with a maximum order of two is applied to meet the requirement and increase the accuracy of the approximation. For handling the linear system of equations at any time-step, PARDISO and MUMPS direct solvers are used.

The computational mesh of the vibrating-rotating cylinder after deformation is depicted in Fig. 2(d), at the 50th second of the simulation time where maximum displacement occurs for the case $U^*=14$. In the outer zone, the mesh shifts linearly, and in the area around the cylinder (outer cylinder), the mesh follows the rotational movement of the cylinder.

In the simulation, while moving near to the surface of the cylinder, the grid size becomes smaller. For the largest flow velocity at $Re=12689$, to keep the y^+ below 5 and increase the accuracy of the boundary layer resolution, the minimum grid size is considered 0.0001. Moreover, based on experience with the present model, the prescribed deformation is assumed at rotating and deforming domains to eliminate the need for re-meshing the model and save time and expenses.

For a vibrating cylinder at $U_r^*=14$ a mesh dependence test is performed, and the number of elements, transverse displacement, mean drag coefficient ($\overline{C_d}$) and the root-mean-square ($C_{l_{RMS}}$) of the lift coefficient are listed in Table 2. Mean Drag and CL_{RMS} are expressed as [37]:

$$\overline{CD}=\frac{1}{N}\sum_{i=1}^{N}\frac{2f_D(t)}{\rho U_{in}^2D} \quad (8)$$

$$CL_{RMS}=\sqrt{\frac{1}{N}\sum_{i=1}^{N}\left[\frac{2f_L(t)}{\rho U_{in}^2D}\right]^2} \quad (9)$$

Fig. 2(e) represents the grid differences around the cylinder. As the grid number increases from G1 to G4, the mesh transition

becomes smoother. The maximum difference between G1 and G2 for calculated parameters is about 5% which reduces to 1.8% for G4 (see Table 2). The simulation time between G4 and G3 on a system with a CPU of 4.2 GHz and 8.0 GB RAM was significant, while the maximum variation in results was near 2%. Therefore G3 with 15078 elements was selected for the rest of the simulations.

3.1 Validation Method

The numerical model in this study is validated against experimental VIV responses by Khalak and Williamson [13] and the numerical by Guilmineau and Queutey [14] for a transversely oscillating cylinder. Simulation parameters, including m^* and ζ are the same as the ones in the above-mentioned experimental and numerical studies (m^* =2.4, $m^*\zeta = 0.0115$). The comparison of the non-dimensional amplitude and frequency responses versus reduced velocity for the vibrating cylinder is presented in Fig. 3. It is found that the amplitude and frequency responses have good agreement with the numerical results of Guilmineau and Queutey [14] for initial, upper, and lower branches. However, the numerical results could not match the upper branch of experimental data of Khalak and Williamson [13]. This is because the *3D* issue was studied in the experiment and two-dimensional simulations employed in this work are not able to capture the vortexes in the critical range of the Reynolds number. Thus, the results of this *2D* numerical simulation are reasonable in regions outside the critical Re range.

The diameter and frequency of the cylinder used in the above-mentioned studies was 38.1 mm, and 0.4 Hz, respectively. The VIV responses from numerical simulation agree well with the experimental results at the lower and initial branches. Moreover, adding the rotational degree of freedom has made the more complex system, and the experimental case of this problem has not been performed yet. Therefore, the same parameters, including the cylinder's diameter and natural frequency, are used in this simulation in order to conveniently compare the VIV response of the vibrating-rotating cylinder with the vibrating one.

(a)

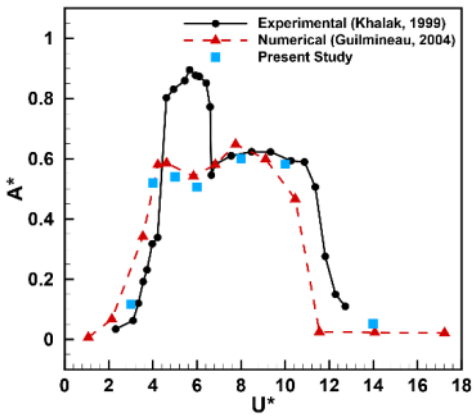

(b)

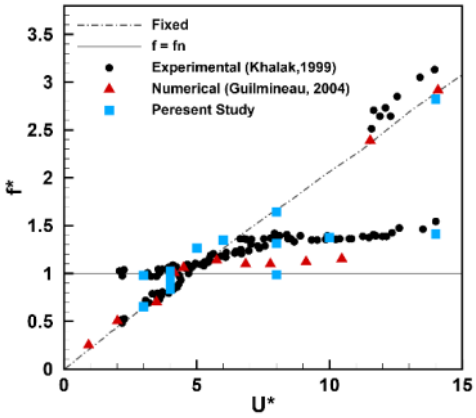

Fig. 3. (a) non-dimensional amplitude response, A^*verses non-dimensional velocity, U^*; (b) non-dimensional frequency response, f^* verses non-dimensional velocity, U^*.

Table 2 Mesh independency test for A^*_{rms}, $\overline{C_d}$ and $C_{l_{RMS}}$ for the vibrating cylinder at $U_r = 14$.

Grid	Elements	A^*_{rms}		$\overline{C_d}$		$C_{l_{RMS}}$	
		Values	Percentage changes	Values	Percentage changes	Values	Percentage changes
G1	7851	0.0277	/	1.667	/	0.137	/
G2	10110	0.0265	4.33%	1.745	4.67%	0.143	4.38%
G3	15078	0.0259	2.26%	1.801	3.21%	0.148	3.49%
G4	32124	0.0256	1.15%	1.823	1.22%	0.150	1.35%

4. Result and Discussions

In this part, the amplitude and frequency responses of the freely vibrating and rotating cylinder for $3 \leq U^* \leq 14$ is presented. The effect of adding a rotational degree of freedom to the vibrating cylinder on the hydrodynamic coefficients, generated power, and energy conversion efficiency at different reduced velocities is discussed in detail.

4.1 Vibration and Rotational Response

Figure 4 displays the transverse displacements and vorticity contours of the vibrating and vibrating-rotating cylinders over a period of oscillation at $U^* = 14$. The nondimensionalized amplitudes are presented in order to facilitate the comparison. It is seen that the displacement of the vibrating-rotating cylinder is significantly greater than (multiple is about 20 times) the vibrating cylinder. The main reason maybe is the larger the pressure difference at the front and rear of the eccentric cylinder due to the rotational motion. Also, the pattern of vortex shedding is changed for the rotational system. For a vibrating-rotating cylinder, the wake pattern becomes wider with a larger size of vorticities. The vortex shedding modes changes from 2P mood, in which four vortices are shed per cycle for the vibrating cylinder to 2S mood, where two vortices are shed per cycle for the vibrating-rotating cylinder. These alterations in vortex shedding moods by adding a rotational degree of freedom cause changes in the acting forces on the cylinder and results in the vibration response increment for the vibrating- rotating cylinder. In addition, the boundary layer near the object's surface is disturbed because of the rotational motion and results in the separation points movement away from the symmetric position around the vibrating cylinder to nonsymmetrical positions for the vibrating-rotating cylinder. Due to the rotation, the locations of separation points change alternatively. When the cylinder moves downward, the separation point goes to the lower half of the cylinder, while for upward motion, the separation point occurs on the upper half of the cylinder.

Figure 5 compares the lift and drag coefficient (C_l, C_d) of the vibrating (1D) and vibrating-rotating (Rotational) cylinders in a certain flow time at maximum reduced velocity $(U^* = 14)$. The cylinder mean drag coefficient $(\overline{C_d})$ is 0.98, and adding a rotational degree of freedom to the system, the amplitude of vibration —as shown in Fig.4— and consequently, the lift and drag coefficients increase and vary with time. This may be caused by the constant changing friction drag and pressure drag under the action of rotation. The mean drag reaches 3.17 in the rotating cylinder due to the enhancement of the vortex-induced vibration effect and changes in the wake pattern. Also, it is seen that despite the harmonic displacement of both vibrating and vibrating-rotating cylinders, nonharmonic lift and drag forces apply on the vibrating-rotating cylinder. This reason may be that skin friction drag does not act tangentially over the surface of the cylinder and enter the geometrical center of the rotating cylinder. Similarly, in the freely vibrating-rotating cylinder, the amplitude of the lift coefficient becomes larger and results in the dimensionless amplitude increment. The root-mean-square of lift coefficient $(C_{l_{RMS}})$ for the vibrating cylinder and the vibrating-rotation cylinder is 0.19 and 1.77 at maximum reduced velocity $(U^* = 14)$, respectively.

The lift force is not the only factor affecting the amplitude response, the natural frequency, inlet velocity, etc., are also important parameters [34]. The movement history of the eccentric cylinder against dimensionless time ($t^* = u_{in}t/D$) is depicted in Fig. 6 for different reduced velocities. By increasing the reduced velocity, non-dimensional displacement increases. Differences in non-dimensional amplitude responses for the lowest and highest reduced velocity are noticeable (increasing from 0.0.5 at $U^* = 3$ to near one at $U^* = 14$). Whereas at higher reduced velocities 9-14, the cylinder experiences a gradual increase in dimensionless amplitude response. As for the rotational response, it does not follow a specific pattern. In all cases, the rotation rate does not reach zero, hence the eccentric cylinder rotates in the counterclockwise direction all the time.

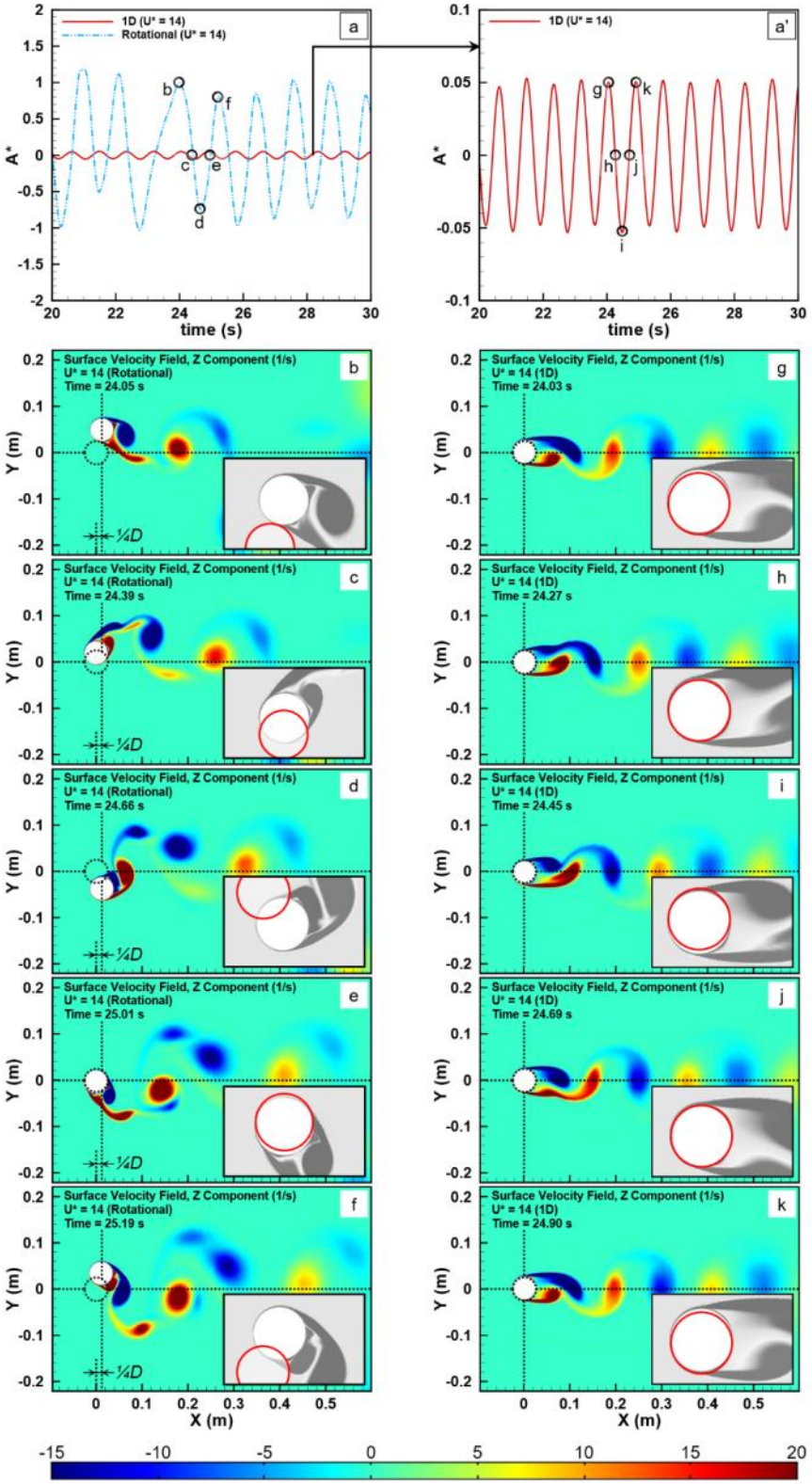

Fig. 4 Vorticity contour for the vibrating and the vibrating-rotating cylinders during the period of oscillation.

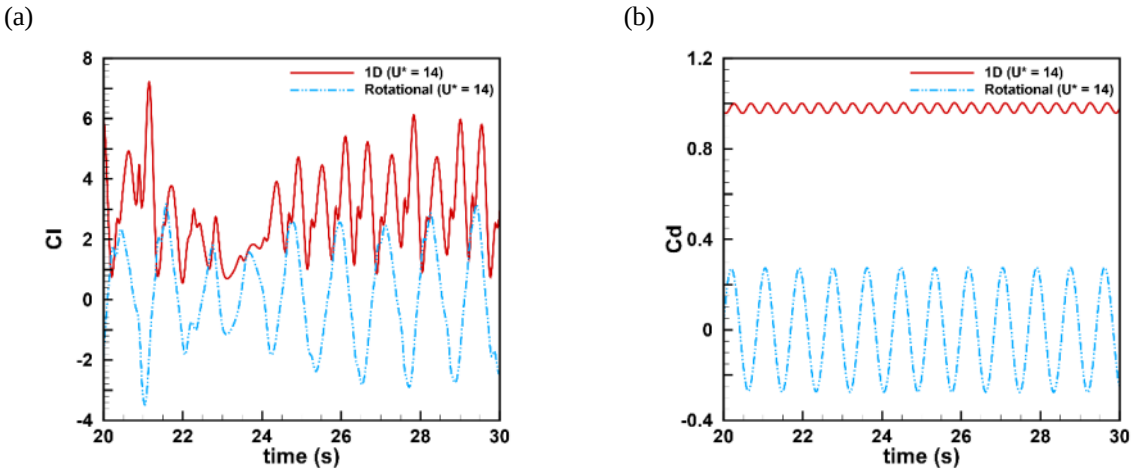

Fig. 5 Comparison of hydrodynamic coefficients (C_d, C_l) of 1D and rotation cylinder at $U^* = 14$.

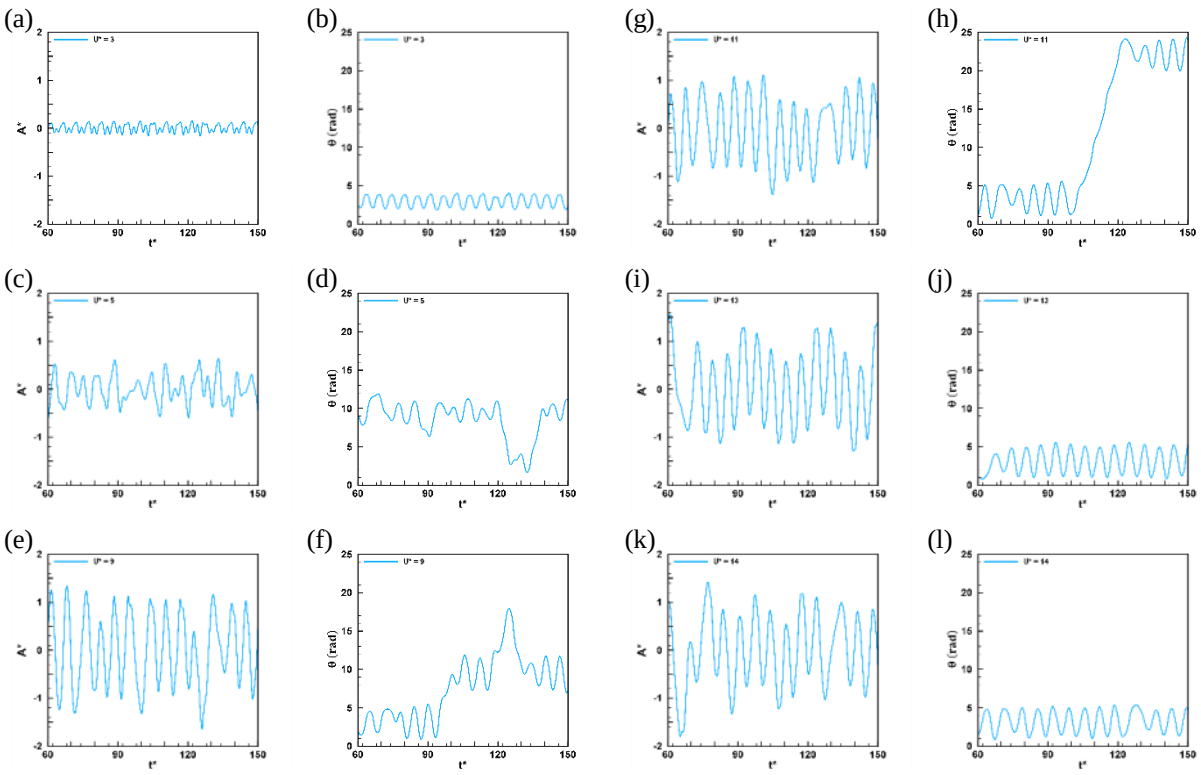

Fig. 6 Non-dimensional amplitude and rotational responses versus non-dimensional flow time; (a, b) $U^* = 3$; (c, d) $U^* = 5$; (e, f) $U^* = 9$; (g, h) $U^* = 11$; (I, j) $U^* = 13$; (k, l) $U^* = 14$.

With the start of counterclockwise rotation, the formed vortex in the lower, followed by pressure difference along the negative transverse direction, pushes the cylinder downward direction. At $U^* = 3$, the cylinder flaps between 2 and 4 radians. At $U^* = 5, 9,$ and 11, the complete rotation of the cylinder can be seen in some flow times, however, for higher reduced velocities, $U^* = 13$ and $U^* = 14$, complete rotation around the center of the rotation occurs at each rotation period. The cycle time of vibration is not consistent with the rotation rate which means that rotation and vibration are not synchronized.

With increasing reduced velocity ($3 \leq U^* \leq 13$), the dominant frequency and the spectrum amplitude increase as well. $U^* = 13$ has a maximum spectrum amplitude but a fewer number of dominant frequencies. For $U^* = 14$, two significant frequencies have nearly the same amplitude of the spectrum and the dominant frequency ratio of 0.89.

The hydrodynamic coefficients ($\overline{C_d}$ and $C_{l_{RMS}}$) of the vibrating-rotating and vibrating cylinders are presented in Fig. 8. It is clearly seen that the vibrating-rotating (Rotational) and vibrating (1D) cylinders have different change trends in the mean drag coefficient. When the reduced velocity increases from 3 to 4, there is a slight change in coefficients. For a vibrating cylinder, for reduced velocity greater than 8, the mean drag coefficient decreases as U^* increases. However, for the vibrating-rotating cylinder, the $\overline{C_d}$ grows rapidly as U^* increases. Compering the mean drag values for $U^* = 13$ and $U^* = 3$, it can be seen that the coefficient is about two times larger. The reason is that increment of the reduced velocity results in shedding the bigger vortices in the wake, and consequently, greater drag force is acted on the object. A motionless circular cylinder at $10^3 < Re < 5 \times 10^5$ has an approximately constant drag coefficient (1~1.2). However, due to fluid and solid interactions, the vibration and rotation enhance the drag coefficient. The freely vibrating-rotating cylinder has a larger drag coefficient at the same reduced velocity ($U^* = 13$) as it has a larger vibration amplitude (Fig. 6(e)) and spectrum amplitude (Fig. 7(e)). The root mean square of the lift coefficient ($C_{l_{RMS}}$) versus reduced velocity for the vibrating-rotating cylinder and the vibrating cylinder do not follow specific trends. However, in general, the $C_{l_{RMS}}$ for the rotational system is larger than the vibrating cylinder. For reduced velocities greater than 8, the root-mean-square of lift coefficients slightly decreases while it grows for the vibrating-rotating cylinder.

Pressure fields and streamlines during the period of displacement for a vibrating cylinder and its counterpart point on the displacement diagram of the vibrating-rotating eccentric cylinder at $U^* = 10$ is given in Fig. 9. The nonharmonic pressure field distribution around the rotational cylinder can be considered the main cause of amplitude variation. It is seen that for the vibrating cylinder, the pressure distribution is symmetrical, and maximum pressure occurs at the stagnation point. However, for the vibrating-rotating cylinder, the pressure distribution is asymmetric, and maximum pressure is not limited to the stagnation point.

4.2 Power Generation and Conversion Efficiency

The mathematical model for harnessed power of the eccentric cylinder has been introduced. The freely vibrating-rotating cylinder generates power in transverse and rotational directions calculated by

$$P1 = \frac{1}{(t - t_s)} \int_{t_s}^{t} f(t).\dot{y}\, dt \tag{10}$$

$$P_{tot} = \frac{1}{(t - t_s)} \int_{t_s}^{t} (f(t).\dot{y} + M(t).\dot{\theta}) dt \tag{11}$$

in which $f(t) = m\ddot{y} + c\dot{y} + ky$, $M(t) = I\ddot{\theta}$, and P_1 is the power generated by the crossflow motion of the cylinder called vibration power while P_{tot} is the total power summation of the vibration power and the rotational power. Transverse velocity ($\dot{y}$), acceleration ($\ddot{y}$), and angular acceleration ($\ddot{\theta}$) can be determined based on the displacement and angular position of the cylinder in each time step. Based on Bernoulli's Equation, the fluid power can be defined as (Eq.10), DL is the projected area of the cylinder [31].

$$P_{fluid} = \frac{1}{2}\rho U u_{in}^3 DL \tag{12}$$

Since there is no significant difference in the sweeping area of either vibrating or vibrating-rotating cylinders, the energy conversion efficiency η of the converter can be generalized to the case of this study and evaluated by

$$\eta = \frac{P_{tot}}{P_{fluid}} \tag{13}$$

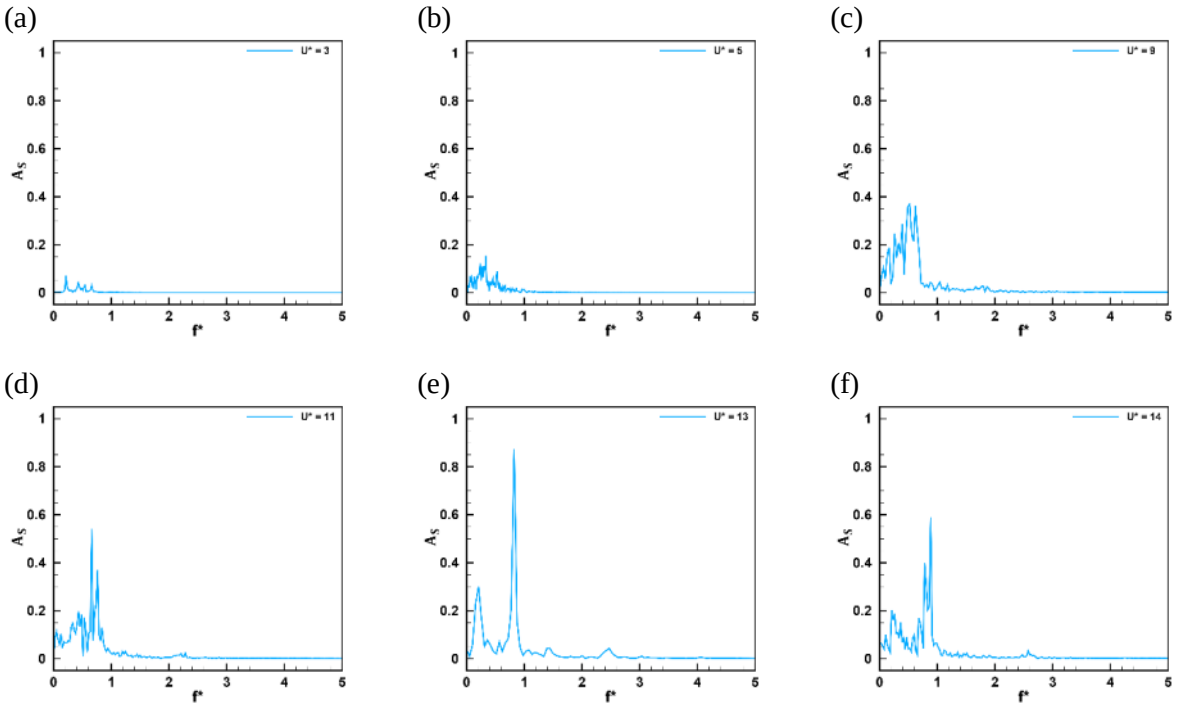

Fig. 7 The amplitude of the spectrum (A_s) versus frequency ratio (f^*); (a) $U^* = 3$; (b) $U^* = 5$; (c) $U^* = 9$; (d) $U^* = 11$; (e) $U^* = 13$; (f) $U^* = 14$.

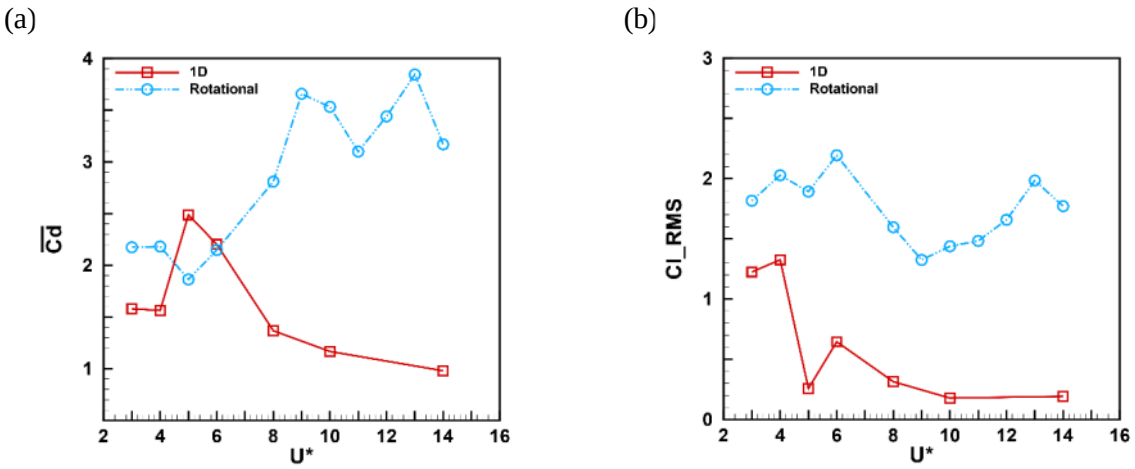

Fig. 8 Comparison of the hydrodynamic coefficient against the reduced velocity for the vibrating-rotating and vibrating cylinders; (a) the mean drag coefficient; (b) the root-mean-square of the lift coefficient.

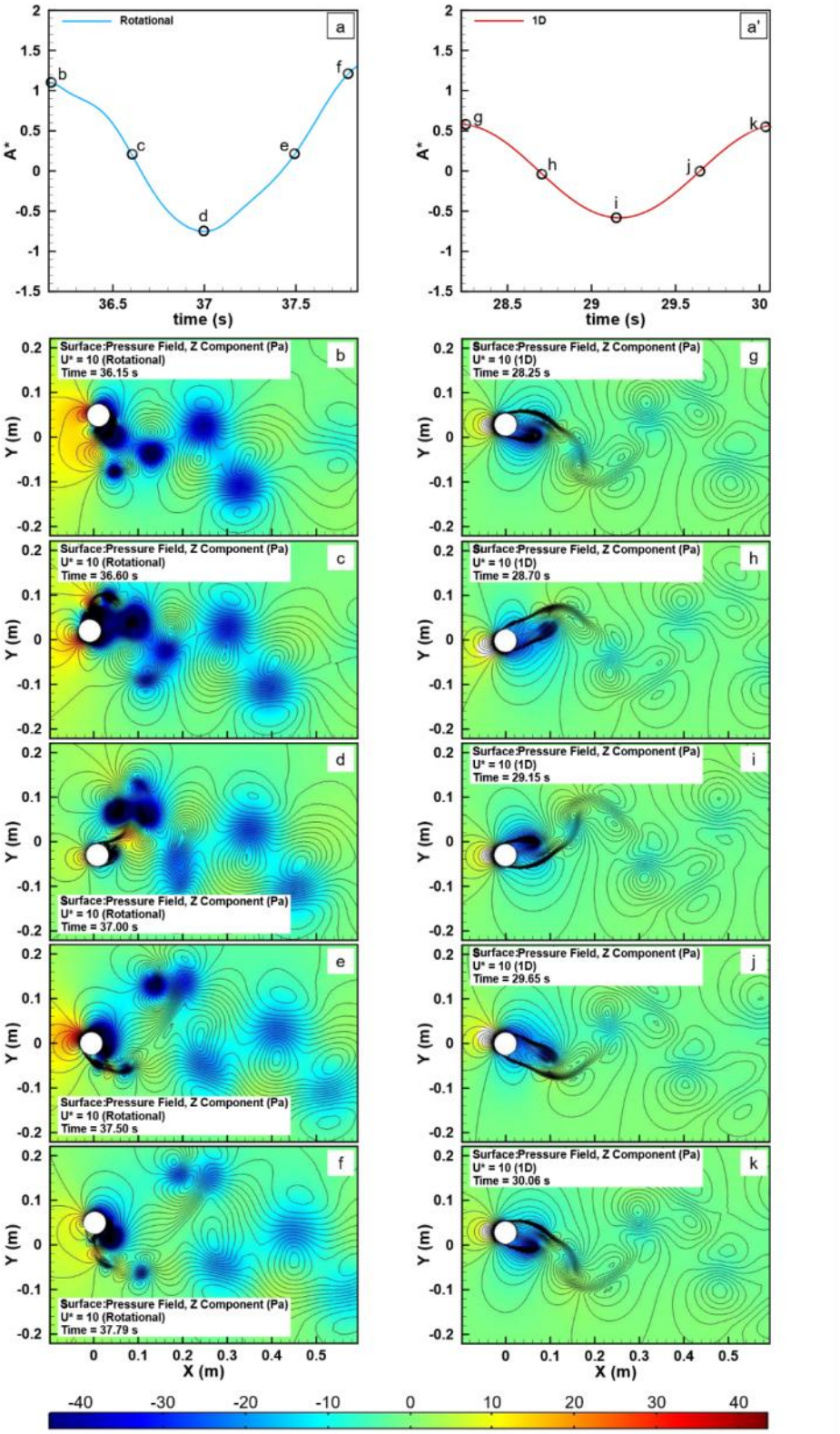

Fig. 9 Pressure fields and streamlines around the cylinder during a period of oscillation for vibrating and vibrating-rotating cylinder at $U^* = 10$.

The generated power from the vibrating (1D) and vibrating-rotating (Rotational) system are displayed in Fig. 10. It can be seen that the power of the freely vibrating-rotating cylinder increases dramatically with increasing reduced velocity. This is because the rotational motion of the cylinder enhances the frequency and amplitude responses so that more energy can be harvested at larger inlet velocities. The maximum power for this study is 0.024 (W) for $U^* = 14$. The vibrational (red line) and total power (blue line) —power harnessed both from rotation and vibration of a cylinder— of the converter are estimated by Eq.8 and Eq.9, respectively. The vibration power of the freely vibrating-rotating cylinder is greater than the rotational one.

Figure 11 shows the energy conversion efficiency of the converter computed by Eq.11 for different reduced velocities. The efficiency generally increases by adding a degree of freedom to the system, especially for higher reduced velocities, differences are noticeable. The efficiency of the vibrating-rotating system experiences some fluctuations at different flow velocities. Here, the average conversion efficiency for the freely vibrating-rotating cylinder is 0.112, which means, unlike the vibrating (1D) system, the efficiency for the rotating converter is independent from reduced velocity.

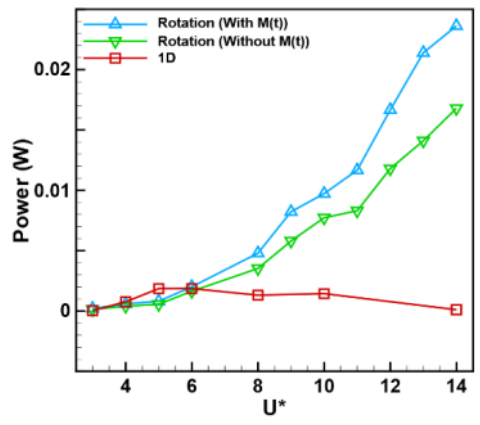

Fig. 10 Comparison of power generated by 1D and vibrating-rotating cylinder versus reduced velocity.

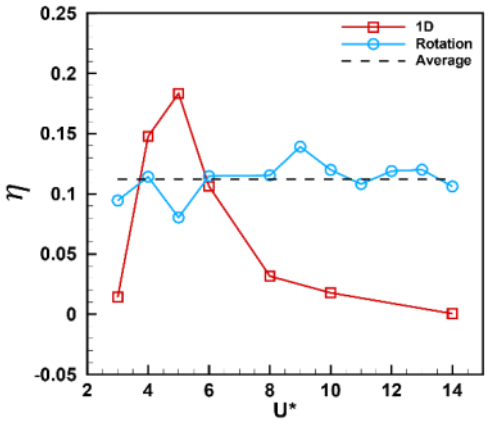

Fig. 11 The power efficiency of the system at different flow velocities.

5. Conclusions

In this study, adding a degree of freedom to the VIV converter is proposed in order to increase the harnessed hydrokinetic power and energy conversion efficiency of the converter with varying Reynolds numbers from 2×10^3 to 13×10^3. The rotational degree of freedom is simply exerted using an elastically mounted eccentric circular cylinder. The URANS equations combined with the *SST* turbulence model are solved on the structured moving mesh, divided into three sub domains.

Prescribed deformation is applied to the rotating and deforming domains to reduce the computational time; deformation of boundaries is calculated by the ALE scheme. Based on the result of the present work, the main finding is listed as

- The vibration amplitude of the freely vibrating-rotating cylinder increases with increasing reduced velocity. Since the displacement history is nonharmonic, the system has more than one dominant frequency. The increase in vibration response and the number of dominant frequencies result in generated power enhancement of the converter.
- The rotational degree of freedom causes hydrodynamic instability. In low inlet velocities, the cylinder flaps between 2 and 4 radians while increasing the velocity the cylinder undergoes complete rotation. Therefore, the wider wake pattern forms

and unstable vortexes shed, leading to the enhancement of vibration response and consequently harnessed power of the converter.

- The hydrokinetic power generated by the freely vibrating-rotating system increases as reduced velocity increases. However, the energy conversion efficiency of the system stays constant and fluctuates around 11.2% for all reduced velocities examined in this study.

Declarations

This research did not receive any specific grant from funding agencies in the public, commercial, or not-for-profit sectors.

References

[1] Asif M, Muneer T. Energy supply, its demand and security issues for developed and emerging economies. Renewable and sustainable energy reviews. 2007;11(7):1388-413.

[2] Al-Habaibeh A, Su D, McCague J, Knight A. An innovative approach for energy generation from waves. Energy Conversion and Management. 2010;51(8):1664-8.

[3] Stiassnie M, Kadri U, Stuhlmeier R. Harnessing wave power in open seas. Journal of Ocean Engineering and Marine Energy. 2016;2(1):47-57.

[4] Ma P, Wang Y, Xie Y, Huo Z. Numerical analysis of a tidal current generator with dual flapping wings. Energy. 2018;155:1077-89.

[5] Gu M, Song B, Zhang B, Mao Z, Tian W. The effects of submergence depth on Vortex-Induced Vibration (VIV) and energy harvesting of a circular cylinder. Renewable Energy. 2020;151:931-45.

[6] Bernitsas MM, Raghavan K, Ben-Simon Y, Garcia EM. VIVACE (Vortex Induced Vibration Aquatic Clean Energy): A new concept in generation of clean and renewable energy from fluid flow. Journal of offshore mechanics and Arctic engineering. 2008;130(4):041101.

[7] Sun H, Ma C, Kim ES, Nowakowski G, Mauer E, Bernitsas MM. Hydrokinetic energy conversion by two rough tandem-cylinders in flow induced motions: Effect of spacing and stiffness. Renewable Energy. 2017;107:61-80.

[8] Ding L, Zhang L, Bernitsas MM, Chang C-C. Numerical simulation and experimental validation for energy harvesting of single-cylinder VIVACE converter with passive turbulence control. Renewable Energy. 2016;85:1246-59.

[9] Raghavan K, Bernitsas MM. Experimental investigation of Reynolds number effect on vortex induced vibration of rigid circular cylinder on elastic supports. Ocean Engineering. 2011;38(5-6):719-31.

[10] Bearman PW. Vortex shedding from oscillating bluff bodies. Annual review of fluid mechanics. 1984;16(1):195-222.

[11] Gabbai RD, Benaroya H. An overview of modeling and experiments of vortex-induced vibration of circular cylinders. Journal of Sound and Vibration. 2005;282(3-5):575-616.

[12] Williamson CHK, Govardhan R. Vortex-induced vibrations. Annu Rev Fluid Mech. 2004;36:413-55.

[13] Khalak A, Williamson CHK. FLUID FORCES AND DYNAMICS OF A HYDROELASTIC STRUCTURE WITH VERY LOW MASS AND DAMPING. Journal of Fluids and Structures. 1997;11(8):973-82.

[14] Khalak A, Williamson CHK. MOTIONS, FORCES AND MODE TRANSITIONS IN VORTEX-INDUCED VIBRATIONS AT LOW MASS-DAMPING. Journal of Fluids and Structures. 1999;13(7):813-51.

[15] Guilmineau E, Queutey P. Numerical simulation of vortex-induced vibration of a circular cylinder with low mass-damping in a turbulent flow. Journal of fluids and structures. 2004;19(4):449-66.

[16] Williamson CHK, Roshko A. Vortex formation in the wake of an oscillating cylinder. Journal of fluids and structures. 1988;2(4):355-81.

[17] Garcia EMH, Bernitsas MM. Effect of damping on variable added mass and lift of circular cylinders in vortex-induced vibrations. Journal of Fluids and Structures. 2018;80:451-72.

[18] Modir A, Goudarzi N. Experimental investigation of Reynolds number and spring stiffness effects on vortex induced vibrations of a rigid circular cylinder. European Journal of Mechanics-B/Fluids. 2019;74:34-40.

[19] Soti AK, Zhao J, Thompson MC, Sheridan J, Bhardwaj R. Damping effects on vortex-induced vibration of a circular cylinder and implications for power extraction. Journal of Fluids and Structures. 2018;81:289-308.

[20] Sun H, Ma C, Kim ES, Nowakowski G, Mauer E, Bernitsas MM. Flow-induced vibration of tandem circular cylinders with selective roughness: Effect of spacing, damping and stiffness. European Journal of Mechanics - B/Fluids. 2019;74:219-41.

[21] Jauvtis N, Williamson CHK. The effect of two

degrees of freedom on vortex-induced vibration at low mass and damping. Journal of Fluid Mechanics. 2004;509:23.
[22] Gsell S, Bourguet R, Braza M. Two-degree-of-freedom vortex-induced vibrations of a circular cylinder at Re=3900. Journal of Fluids and Structures. 2016;67:156-72.
[23] Gsell S, Bourguet R, Braza M. One- versus two-degree-of-freedom vortex-induced vibrations of a circular cylinder at Re=3900. Journal of Fluids and Structures. 2019;85:165-80.
[24] Pastrana D, Cajas JC, Lehmkuhl O, Rodr ́guez I, Houzeaux G. Large-eddy simulations of the vortex-induced vibration of a low mass ratio two-degree-of-freedom circular cylinder at subcritical Reynolds numbers. Computers & Fluids. 2018;173:118-32.
[25] Mittal S. Flow past rotating cylinders: effect of eccentricity. J Appl Mech. 2001;68(4):543-52.
[26] Srigrarom S, Koh AKG. Flow field of self-excited rotationally oscillating equilateral triangular cylinder. Journal of fluids and structures. 2008;24(5):750-5.
[27] Lu L, Guo X-l, Tang G-q, Liu M-m, Chen C-q, Xie Z-h. Numerical investigation of flow-induced rotary oscillation of circular cylinder with rigid splitter plate. Physics of Fluids. 2016;28(9):093604.
[28] Wang H, Zhai Q, Chen K. Vortex-induced vibrations of an elliptic cylinder with both transverse and rotational degrees of freedom. Journal of Fluids and Structures. 2019;84:36-55.
[29] Barrero-Gil A, Pindado S, Avila S. Extracting energy from vortex-induced vibrations: a parametric study. Applied mathematical modelling. 2012;36(7):3153-60.
[30] Zheng M, Han D, Gao S, Wang J. Numerical investigation of bluff body for vortex induced vibration energy harvesting. Ocean Engineering. 2020;213:107624.
[31] Ding L, Zhang L, Wu C, Mao X, Jiang D. Flow induced motion and energy harvesting of bluff bodies with different cross sections. Energy Conversion and Management. 2015;91:416-26.
[32] Zhang B, Wang K-H, Song B, Mao Z, Tian W. Numerical investigation on the effect of the cross-sectional aspect ratio of a rectangular cylinder in FIM on hydrokinetic energy conversion. Energy. 2018;165:949-64.
[33] Zhang LB, Dai HL, Abdelkefi A, Wang L. Experimental investigation of aerodynamic energy harvester with different interference cylinder cross-sections. Energy. 2019;167:970-81.
[34] Zhang B, Mao Z, Song B, Ding W, Tian W. Numerical investigation on effect of damping-ratio and mass-ratio on energy harnessing of a square cylinder in FIM. Energy. 2018;144:218-31.
[35] Zhang B, Song B, Mao Z, Tian W, Li B. Numerical investigation on VIV energy harvesting of bluff bodies with different cross sections in tandem arrangement. Energy. 2017;133:723-36.
[36] Zhu H, Gao Y. Vortex induced vibration response and energy harvesting of a marine riser attached by a free-to-rotate impeller. Energy. 2017;134:532-44.
[37] Zhu H, Zhao Y, Zhou T. CFD analysis of energy harvesting from flow induced vibration of a circular cylinder with an attached free-to-rotate pentagram impeller. Applied Energy. 2018;212:304-21.
[38] Donea J, Giuliani S, Halleux J-P. An arbitrary Lagrangian-Eulerian finite element method for transient dynamic fluid-structure interactions. Computer methods in applied mechanics and engineering. 1982;33(1-3):689-723.
[39] Menter FR. Two-equation eddy-viscosity turbulence models for engineering applications. AIAA journal. 1994;32(8):1598-605.
[40] Tahani M, Rabbani A, Kasaeian A, Mehrpooya M, Mirhosseini M. Design and numerical investigation of Savonius wind turbine with discharge flow directing capability. Energy. 2017;130:327-38.
[41] Menter FR, Kuntz M, Langtry R. Ten years of industrial experience with the SST turbulence model. Turbulence, heat and mass transfer. 2003;4(1):625-32.